In situ characterization of the phase diagram of Ir *via* X-ray diffraction coupled with resistive and laser-heated diamond anvil cell

Check for updates

Simone Anzellini [1] ✉, Pablo Botella[1], Jose Luis Rodrigo-Ramon[1], Aser Garcia-Beamud[1], Josu Sanchez-Martin[1], Gaston Garbarino[2], Angelika D. Rosa [2], Samuel Gallego-Parra [2,4], Egor Koemets[3] & Daniel Errandonea [1]

Transition metals, including Iridium, are crucial for understanding planetary cores and developing critical technologies due to their unique properties under extreme high-pressure and high-temperature conditions. Although Ir's room-temperature phase remains stable, its pressure-temperature phase diagram is largely unknown, with only a single experimental melting point reported previously. A notable gap in knowledge is the lack of experimental evidence for solid-solid phase transitions predicted by theoretical models. Here we show a new investigation into the phase diagram of iridium, employing a combination of resistive-heated and laser-heated diamond anvil cells coupled with synchrotron X-ray diffraction. Our findings confirm that Ir maintains its face-centered cubic structure up to 101 GPa and 5600 K. We determined five new melting points that corroborate computational predictions, providing a more robust foundation for the melting curve. The resulting thermal equation of state offers a definitive dataset that can serve as a reliable pressure standard and advance the design of technologies using Ir.

Transition metals display a wide range of fascinating and practically useful characteristics, mainly due to their partially filled *d*-electron bands. Their electronic arrangement results in the delocalization of their *d*-orbitals, which significantly affects their behavior. Consequently, the investigation of their melting curves and the solid-solid structural transformations they undergo under high-pressure (*HP*) and high-temperature (*HT*) conditions is of paramount importance across various scientific disciplines, including physics, materials science, and geophysics[1–4].

Within geophysics, such studies are particularly crucial for developing a deeper understanding of the internal structure and chemical composition of planetary cores. Furthermore, this knowledge is essential for constructing accurate models of planetary interiors, which are vital for estimating the composition of exoplanets classified as super-Earths[5–9]. Beyond fundamental science, transition metals also play a pivotal role in numerous technological applications, notably in the manufacturing of critical components for nuclear reactors, power generation facilities, and turbines. For the efficient and safe design of these technologies, a precise understanding of the *HP-HT* phase

diagrams of transition metals is essential. Driven by these scientific and technological imperatives, the behavior of transition metals under extreme *HP-HT* conditions has been the subject of extensive research for many decades.

Iridium (Ir), is a *5d* transition metal with an electronic configuration of [Xe]4f^{14}5d^{7}6s^2. Among the *5d* transition metals, it shows the highest resistance to compression. It's the second densest element, with a density of 22.56 g/cm^3 and, at ambient conditions it presents a face-centered cubic (*fcc*) structure. Iridium is known for its high thermal stability, strength (due to large shear and bulk moduli), and corrosion resistance, which make it useful for specialized applications like nuclear-powered generators in space technology.

Early high-pressure research on iridium, such as the work by Cerenius et al.[10] at the start of the 21st century, reported on the metal's behavior up to 65 GPa. Using energy-dispersive X-ray diffraction (XRD), they observed changes in the diffraction patterns at 59 GPa. The researchers interpreted these changes as the emergence of a 14-layer hexagonal close-packed (*hcp*) superlattice, a structure similar to one proposed for platinum (Pt), iridium's neighbor on the periodic table, under *HP-HT* conditions[11]. Subsequent

[1]Department of Applied Physics - Institute of Materials Science, Matter at High Pressure (MALTA) Consolider Team, University of Valencia, Burjassot, Valencia, Spain. [2]European Synchrotron Radiation Facility, Grenoble, France. [3]Diamond Light Source Ltd., Harwell Science and Innovation Campus, Didcot, Oxfordshire, UK. [4]Present address: Instituto de Diseño para la Fabricación y Producción Automatizada, MALTA Consolider Team, Universitat Politècnica de València, Valencia, España. ✉e-mail: simone2.anzellini@uv.es

Fig. 1 | Textural evolution. Image plates showing the textural evolution observed at around 26 GPa for Ir and KCl as a function of T. Specifically, at **a** 1930 K, **b** 2887 K, **c** 3250 K and **d** 3477 K.
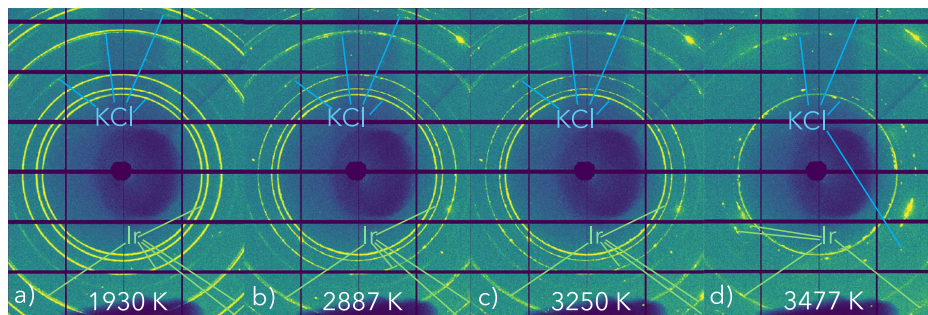
studies, however, both experimental[12] and theoretical[13], were unable to confirm the existence of this phase transition. On the other hand, later studies suggested that iridium undergoes pressure-induced changes in its electronic structure, specifically related to a core-level crossing transition (CLC)[14]. Computational work supported this hypothesis, predicting CLC for Ir to occur at around 80 GPa[15]. Nevertheless, recent findings from static high-pressure diffraction experiments, coupled with theoretical studies[12,16] on the compression behavior of Ir up to 159 GPa, found no evidence of such transition. Furthermore, first-principles calculations[16] now suggest that CLC in Ir is more likely to occur at a considerably higher pressure, around 400 GPa, rather than 80 GPa. Based on existing research, including XRD studies[12,16], computational modeling[13,17], and shock-wave experiments[18], the current consensus is that iridium's *fcc* structure remains stable at room temperature, even at pressures up to 600 GPa.

Numerous experimental[12,14,16,19–21] and theoretical[13,17,22] efforts have also been dedicated to establish an accurate room-temperature equation of state (EoS) for Ir. A comprehensive analysis of all available results[20], utilizing a plot of the pressure derivative of the bulk modulus (K'_0) against the bulk modulus (K_0) including confidence ellipses from the fits, yields the most accurate parameters as $K_0 = 360(5)$ GPa and $K'_0 = 6.0(5)$. Shock wave studies have been used to investigate the mechanical properties of iridium at multi-megabar pressures[23]. These investigations showed that the shear stresses supported by various metals under such extreme conditions are much different from those at ambient conditions. For some metals, these stresses can reach 900 GPa at a pressure of 300 GPa.

On the other hand, our current understanding of Ir *HP-HT* phase diagram is extremely limited. In particular, a phase transition was predicted to happen at around 2000 K and 150 GPa from the *fcc* to a random-disordered hexagonal close-packed (*rhcp*) structure[13]. Experimentally, to the best of our knowledge, only a previous work from our group, performed using laser-heated diamond anvil cell (LH-DAC) combined with synchrotron XRD, reported an in situ investigation of the phase diagram of Ir in a P–T range between 20 and 40 GPa and from ambient up to 4000 GPa[20]. In this work, we were able to obtain a single melting point at 40.3 GPa and extract the radial distribution function of liquid Ir at that conditions. Additionally, a pressure-volume-temperature (P–V–T) thermal equation of state, valid up to 3100 K, was reported[20] with findings consistent with the results of recent computational studies[24,25]. So far, most of iridium's phase diagram is unexplored. Specifically, there is no experimental proof of any solid-to-solid phase transitions caused by changes in pressure and temperature. Additionally, a proper anchoring of its melting line is still missing, a single melting point is not enough to confirm the theoretical simulations.

For these reasons, we decided to perform a new characterization of the melting curve (and phase diagram) of Ir using a combination of a resistive-heated diamond anvil cell (RH-DAC) and a LH-DAC coupled with synchrotron XRD.

Results and discussion
Phase diagram
The *HP-HT* experiments were conducted following the methodology detailed in the Methods section. These experiments involved the collection of data from eight laser-heating ramps and two RH XRD isothermal
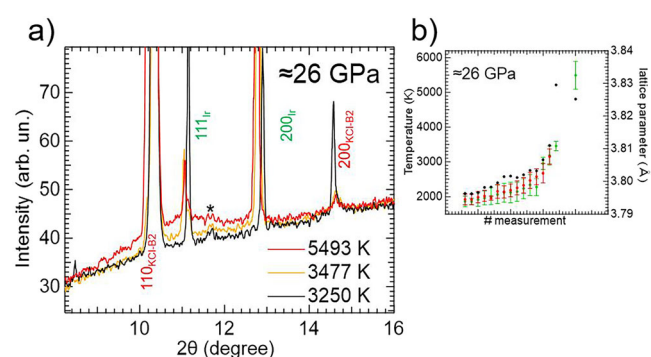

Fig. 2 | Melting onset. a Integrated XRD patterns for increasing T around 26 GPa. At 3250 K (black pattern), Ir still appears in its solid phase. The onset of melting, characterized by the first appearance of the diffuse signal, is observed at 3477 K (yellow). At higher T (5493 K, red pattern), it is possible to observe a change in the diffuse signal, that we attribute to the presence of a mixture of liquid/solid KCl as well as Ir. The black asterisk indicates the peak obtained from the Re gasket, caused by the large tails in the X-ray beam of I15. **b** Red and green circles represent the T measured from the upstream and downstream side of the sample, respectively. The black circle represent the lattice parameter of *fcc*-Ir.

compressions, spanning a pressure-temperature range of up to 101 GPa and 5600 K, respectively. Within this investigated P–T range, only the *fcc* solid phase of Ir and the solid phases of the pressure-transmitting medium (PTM) the B2 phase of KCl and the B1 phase of MgO, were observed.

A generally consistent temperature-induced textural evolution was observed across all heating ramps. Figure 1 illustrates an example of this evolution at approximately 26 GPa. Specifically, at 1930 K (Fig. 1a), powder diffraction patterns were evident for both Ir and KCl. The larger peaks observed for B2-KCl, compared to those of *fcc*-Ir, are attributed to the differing thicknesses of the two materials. Upon increasing temperature, the diffraction signal from the KCl used as PTM remained relatively stable. In contrast, the progressive grain growth of Ir was discernible through the evolution from a powder-like pattern (characterized by Debye-Scherrer rings) to a more textured pattern, exhibiting a combination of large, single-crystal-like spots and a highly oriented powder XRD pattern.

In contrast to observations reported for other transition metals[3,26,27], the phenomenon of "fast recrystallization," characterized by the disappearance and reappearance of single-crystal spots belonging to the same crystallographic planes at varying azimuthal angles during each measurement, typically detected several hundred degrees before melting, was not observed. This is likely to be attributable to the radial thermal gradients probed by the relatively large X-ray beam at the I15 beamline of Diamond Light Source. This factor also explains the observation of a mixed phase exhibiting both a highly oriented powder pattern and large single-crystal spots, rather than a clear transition from one to the other. Finally, with further temperature increases in four of the ramps performed, the emergence of a diffuse halo was observed, which is indicative of a liquid phase (see Figs. 1 and 2). The simultaneous presence of liquid and solid phases in a single-component system is a direct consequence of thermal gradients. Specifically, axial
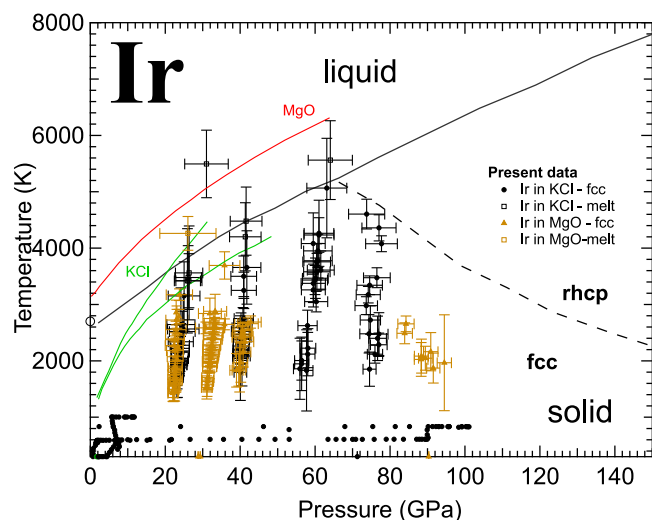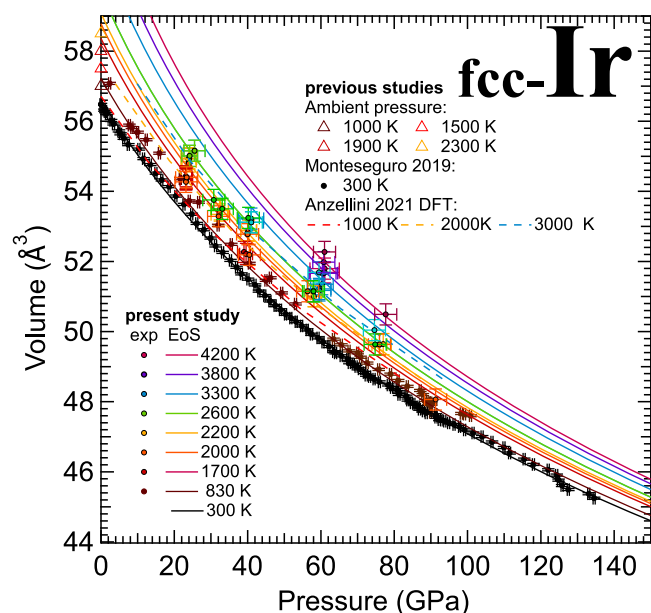
Fig. 3 | P–T phase diagram. Phase diagram of Ir as obtained from the experimental data acquired in this study, together with the phase diagram proposed by Bur-akovsky et al.[13] and the melting curves of MgO[31] and KCl[32,33]. The experimental data points are color-coded according to the PTM employed: black for KCl and gold for MgO. The dashed black line represents the theoretically predicted phase boundary between the *fcc* and the *rhcp* phases of Ir. The empty black circle represents Ir melting point at ambient *P* as reported in Young[55].

Fig. 4 | Thermal EoS. Compression curves of *fcc*-Ir along different isotherms. Temperatures are color-coded as in the legend. The solid lines are the isothermal compression curves calculated according to the thermal equation of state established in the present study. Empty triangles are from experimental thermal expansion point of Rh at ambient *P*. Dashed lines are from previous DFT simulations[20].

thermal gradients on the order of hundreds of K per μm are created by laser heating the sample's surface. Given the sample's thickness of 5–10 μm, these gradients cause the XRD patterns to exhibit a mixed signal, with the liquid phase detected at the hotter surfaces and the solid phase from the cooler inner regions. Generally, with subsequent temperature increases above the melting point, the relative intensity of the diffuse signal compared to the solid diffraction peaks increases as a larger fraction of the inner parts of the sample melts[28–30]. However, in the current study, this specific behavior was not observed. On the other hand, Fig. 2 illustrates a distinct evolution of the diffuse scattering signal. In the orange pattern, attributed to the melting of Ir, the diffuse signal spans from 9.3° to 13° in 2θ, with a maximum intensity at approximately 11.4°. Conversely, at 5493 K (red pattern in Fig. 2), the diffuse signal extends from 8.4° to 13° in 2θ with its maximum shifting to around 10.5°. This change is likely due to the melting of KCl-B2, as we will explain below. Consequently, the final diffraction pattern repre-sents a superposition of partially molten Ir and partially molten KCl. A similar phenomenon was also noted in an experiment focused on char-acterizing the melting curve of Cr, where the evolution progressed from the melting of Cr alone to the concurrent melting of Cr and KBr (the PTM employed)[30].

Figure 3 presents the experimental data acquired in this study, together with the phase diagram proposed by Burakovsky et al.[13] and the melting curves of MgO[31] and KCl[32,33]. The experimental data points are color-coded according to the PTM employed: black for KCl and gold for MgO. It is important to point out that the presence of thermal gradients does not affect the determination of the melting temperature beyond the experimental error. This is confirmed by several factors, including the high accuracy of the spectral radiometric measurements, the fact that T is measured at the sample's hottest parts (the surfaces), and the XRD technique's melting detection limit, which has a precision of approximately 2–3 wt.%[34] (probably 6–7 wt.% in a diamond anvil cell).

Analysis of the data in Fig. 3 yields three primary insights. First, the determined melting points exhibit good agreement, within experimental uncertainties, with both the melting line and the solid phase diagram pre-dicted by density-functional theory (DFT) simulations[13,20]. Second, con-sidering the two reported melting curves for KCl, our experimental results, consistent with the observations for Fig. 2, strongly suggest a higher melting curve for KCl, aligning with the extrapolation from the piston-cylinder

experiment by Pistorius[33] and with the extrapolation of differential thermal analysis measurements made up to 10 GPa[35]. Finally, examination of the data points obtained using MgO as the PTM and insulating material from diamond anvils reveals a limitation in achieving experimental temperatures above 3000 K. Specifically, during each heating ramp, either it was not possible to elevate the sample temperature beyond approximately 2800 K (regardless of laser power), or the sample exhibited an abrupt temperature increase of the order of 1000 K after several increments in laser power. This same behavior was also observed in our prior investigation of Ir, where the use of MgO as an insulating material hindered sustained high-temperature heating, ultimately leading to a sudden temperature surge and the appear-ance of a significant diffuse signal from Ir in the X-ray diffraction pattern[20]. We noticed an analogous behavior in previous works employing MgO as an insulating material when studying the melting curve of other metals. We attribute this to the higher thermal conductivity of MgO ($60 \, Km^{-1}K^{-1}$) compared to KCl ($6 \, Km^{-1}K^{-1}$)[36,37].

Equation of state

Figure 4 shows the volumes measured for *fcc*-Ir at *HP-HT* and the resulting compression curves along different isotherms. Starting from the presented data it was possible to establish the *P–V–T* equation of state (EoS) for Ir using the EOSfit software suite[38]. According to the formalism described in Angel et al.[38], when *T* is involved, the final *P* can be expressed as:

$$P(V, T) = P(V, 300K) + P_{Th}(T) \qquad (1)$$

where $P(V, 300\,K)$ is the isothermal EoS of the material at ambient *T* and $P_{Th}(T)$ the thermal pressure. In the present work, $P(V, 300K)$ was calculated from the data reported by Monteseguro et al.[12], while P_{Th} was modeled following Holland and Powell:

$$P_{Th}(T) = \alpha_0 K_0 \frac{\Theta_E}{\zeta_0} \left(\frac{1}{exp(\Theta_E/T) - 1} - \frac{1}{exp(\Theta_E/300) - 1} \right) \qquad (2)$$

where Θ_E is the Einstein *T* of the material (298 K for Ir), K_0 is the bulk modulus obtained from the isothermal EoS at ambient *T*, α_0 is the thermal

Table 1 | EoS comparison: EoS parameters obtained in the present and in previous experiments

V_0 (Å³)	K_0 (GPa)	K'_0	$\alpha_0 \times 10^{-5}$ (K⁻¹)	Model	Method	PTM
56.62(5)	327(2)	5.46(3)	1.87(8)	BM3+HP	AD-XRD	KCl+He
56.48(9)	360(5)	6.0(5)	1.6(2)	BM3+Ber	AD-XRD[20]	MgO
56.48	339(3)	5.3(1)		BM3	AD-XRD[12]	He
56.58	383(14)	3.1(8)		BM3	AD-XRD[19]	Ar
56.64(24)	341(19)	4.7(3)		BM3	AD-XRD[14]	Ne
56.69	306(23)	6.8(2)		BM3	ED-XRD[10]	MgO
56.614(13)	353(3)	5.03(9)		BM3	AD-XRD[16]	Bi
56	385	5.25		Vinet	DFT[16]	
56.58	366	5		BM3	DFT[13]	
56.17	377	5.3		Vinet	DFT[20]	

In the table, we are indicating the methodology used: AD and ED stand for angular or energy dispersive XRD; DFT: Density-functional theory. We are also indicating the PTM used in the experiments and the EoS model adopted: BM3: 3rd order Birch-Murnaghan; HP: Holland and Powell; Ber: Bermann equation. For the present experiment, we have indicated KCl+He because we have used previously reported data from[12] for the ambient T part that were collected in He, while our data (collected in KCl) for the thermal part.

expansion coefficient at 300 K and ζ_0 is expressed as:

$$\zeta_0 = \frac{(\Theta_E/300)^2 exp(\Theta_E/300)}{(exp(\Theta_E/300) - 1)^2} \quad (3)$$

As shown in Fig. 4, the experimental data, averaged over temperature ranges of ±100 K, are well-described by a third-order Birch-Murnaghan EoS and a thermal pressure model based on the expression by Holland and Powell. Further confirmation of that can be found in Supplementary Fig. 5 where we are reporting the corresponding fit correlation map. The best-fit parameters for this model are $V_0 = 56.62(5)$ Å³; $K_0 = 327(2)$ GPa; $K'_0 = 5.46(3)$ and $\alpha_0 = 1.87(8) \times 10^{-5}$ K⁻¹ These values are summarized in Table 1 for comparison with previous studies.

The present results show excellent agreement with prior thermal expansion measurements of Ir at ambient pressure, as indicated by the empty triangle in Fig. 4. Moreover, the thermal expansion coefficient reported here agrees within one standard deviation with the value determined from experiments up to 48 GPa and 3100 K[20].

Finally, a notable observation is the behavior of the theoretical DFT calculations. While previous DFT results at ambient pressure show volumes that are 2% lower than the experimental values[20], the theoretical isothermal values at 2000 K and 3000 K align well with the experimental data obtained in the present study across the investigated P–T range.

The values determined for the EoS parameters, V_0, K_0, and K'_0, show excellent agreement with previous studies. Specifically, the value for V_0 is consistent with prior works (see Table 1). The correlated parameters, K_0, and K'_0, fall within the 68.3% confidence ellipse of results reported by Monteseguro et al.[12], Yusenko et al.[14], Storm et al.[16], and Anzellini et al.[20].

The minor differences observed between the studies can be attributed to the use of different pressure media and investigated pressure ranges. The comparisons in Table 1 further confirm that the results from Cynn et al.[19] overestimate K_0 and underestimate K'_0, and that Cerenius et al.[10] reported an underestimated value for K_0.

In summary, the combined evidence supports the conclusion that the present P–V–T EoS provides an accurate description of how the volume of iridium changes with pressure and temperature.

Conclusions

This research systematically investigates iridium's phase diagram at high pressure and temperature, with experiments conducted up to 101 GPa and 5600 K. To the best of our knowledge, the study expands the known experimental range for this material. The obtained findings demonstrate that in the investigated pressure-temperature range, iridium consistently maintains its fcc structure. Furthermore, five melting points were precisely

Table 2 | Triad systematics: Thermo-elastic constants of the Co triad as reported in the literature from experiment performed using similar techniques and compared to the present results for Ir

shell	element	K_0 (GPa)	K'_0	$\alpha_0 \times 10^{-5}$ (K⁻¹)
3d	Co[29]	194(2)	3.73(3)	2.897(8)
4d	Rh[54]	257(3)	5.35(2)	2.050(12)
5d	Ir	327(2)	5.46(3)	1.87(8)

determined, which independently corroborate prior computational predictions.

This comprehensive experimental dataset provides a strong rationale for future investigations that push beyond the 101 GPa pressure limit. Specifically, it encourages the search for the theoretically predicted $rhcp$ solid phase, which computational models suggest may exist at higher pressure and temperature conditions. Finally, a definitive pressure-volume-temperature EoS for iridium was established. This P−V−T EoS, whose results are in good agreement with previous calculations[20] in the experimental P–T range, is a critical contribution. In fact, it provides important information for the advancement of numerous technological applications leveraging the unique properties of iridium, as well as enhancing its utility as a reliable pressure standard in demanding HP-HT research environments.

Comparing the thermo-elastic properties of iridium with other elements in its triad reveals a clear systematic trend: bulk modulus increases as you move from 3d to 5d metals, while the thermal expansion coefficient decreases with an increasing number of electron shells (as detailed in Table 2). In fact both parameters are inversely related. It should be noted here that in Table 2, $\alpha_0 \times K_0$ does not change much from one element to the other, with a value of 568(55) 10⁻⁵ K⁻¹ GPa.

Our hypothesis is corroborated by comparing the thermo-elastic properties of elements from neighboring columns of the periodic table to those in the Co column. The results in Table 2 can be compared with Pt and Rh, two elements with known thermo-elastic properties. For instance, platinum (to the right of iridium) shows thermo-elastic properties $K_0 = 274(3)$ GPa, $K'_0 = 4.7(1)$ and $\alpha_0 = 2.26(9) \times 10^{-5}$ K⁻¹ [27,39] similar to Rh. In the case of Pt $\alpha_0 \times K_0 = 619(12)$ 10⁻⁵ K⁻¹ GPa. Conversely, Ru, which is to the left of Rh, shows $K_0 = 323(5)$ GPa, $K'_0 = 4.1(1)$ and $\alpha_0 = 1.91(7) \times 10^{-5}$ K⁻¹ [40]. In this case, the product is $\alpha_0 \times K_0 = 616(18)$ 10⁻⁵ K⁻¹ GPa. These observations support the conclusion that similar bulk moduli are often linked to similar thermal expansion coefficients. The assumption that the product $\alpha_0 \times K_0$ is constant appears to be a crude but effective approximation for late transition metals, even if a direct trend based solely on occupied electron shells is not immediately apparent across the periodic table.

Methods

Sample preparation

The totality of the data reported were collected from two synchrotron radiation facilities using different heating techniques: resistive- and laser-heating. In both cases, the same sample preparation was adopted. In particular, membrane DACs (Letoullec type[41]) were equipped with beveled diamonds with a Boehler-Almax design[42] and culets diameters ranging from $100\,\mu m$ to $300\,\mu m$. Re foils were used as gasket materials: pre-indented and laser-drilled to obtain a high-pressure chamber. The thickness of the pre-indented gaskets and the diameter of the high-pressure chamber's hole were adjusted based on the culet diameter of the diamond used. Specifically, gasket thickness ranged from $30\,\mu m$ (for $300\,\mu m$ culets) to $25\,\mu m$ (for $100\,\mu m$ culets). The chamber's hole was drilled to a diameter half that of the culet (e.g., $150\,\mu m$ for a $300\,\mu m$ culet). Samples were obtained from Ir powder sourced from Goodfellow (99.9% purity). Grains of the powder sample were compressed between two diamond anvils in order to create a foil. The obtained foil, $5-10\,\mu m$ thickness, was then cut and loaded in the DAC high-pressure chambers between either two magnesium oxide (MgO) or potassium chloride (KCl) disks. The MgO and KCl disks, acting as insulating material (both thermally and chemically) and pressure-transmitting medium, as well as pressure gauge, were oven dried at 200 °C for at least two hours before being loaded in the DAC to remove any water or moisture.

Experimental setup

The resistive heating experiments were performed at the extreme conditions beamline ID15B[43] of the ESRF (European Synchrotron Radiation Facility), were the X-rays were tuned to 30 keV and focussed down to $5 \times 5\,\mu m^2$. XRD signals were collected on the beamline's large area EIGER2 X 9M CdTe (340×370 mm) flat panel detector. Whereas, the laser-heating experiment were performed at the extreme conditions beamline I15 at Diamond Light Source Ltd.[44], where the X-rays were tuned to and focused down to $6 \times 9\,\mu m^2$ (Full Width Half Maximum). The scattered XRD signal was collected on a CdTe Pilatus2M detector. In both cases, the sample-to-detector distance were obtained from the XRD signal of a Si standard, following standard procedure and using the calibration routine of the DIOPTAS software suite[45]. The RH-DAC ramps were performed using the internal resistive-heaters developed at the ESRF[46]. The currents passing through the heaters mounted on each seat of the cell were regulated using an eurotherm controller connected to a power supply. The temperatures at the culet and on the back plates of each diamond were monitored using K-type thermocouples, with each diamond having its own K-type thermocouple. In this case, the P inside the cell was measured from the thermal equation of state of either KCl-B2 as reported in Dewaele et al.[47] or MgO as reported in Speziale et al.[48] under the hipothesis that both the PTM and Ir were experiencing the same T. Such an assumption is quite reliable considering the nature of the internal RH-DAC experiment[49,50].

The LH-DAC experiments were performed using the I15 laser-heating system[44], following the methodology detailed in Anzellini et al.[30] A schematic of the adopted system can be found in Supplementary Fig. 1 as well as in Anzellini et al.[30]. Before each heating cycle, the sample was compressed to a target P determined from the compression curve of either KCl or MgO. To minimize temperature variations along the sample's axis, heating was applied from both sides using two 100 W Nd:YAG lasers. Each laser was individually focused on the sample surfaces and adjusted to achieve similar T. The lasers were intentionally slightly de-focused (towards the sample) and overlapped to broaden the full width at half maximum (FWHM) of their Gaussian profiles on the sample surfaces, thereby maximizing the uniformly heated region ($\sim 40\,\mu m$) probed by the X-rays. During the experiment, T was measured using spectral radiometry (between 450 and 950 nm) under the gray body approximation, as described in Anzellini et al.[29] Temperature data were simultaneously acquired from both sides of the sample, and the final T was taken as the average of these two values. The estimated error in each T measurement was the larger of either the T difference between the two sides or the standard deviation of the histograms from their two-colors pyrometry[49]. The corresponding thermal P was derived from the thermal EoS of Dewaele et al.[47] and Speziale et al.[48], assuming that Ir and the PTM experienced the same T. Given the sample geometry and the resulting axial thermal gradient, the maximum error in P was calculated as half the difference between the pressure of the PTM at the measured T (when in contact with Ir) and its pressure at ambient T (when in contact with the diamond). Before and after each heating cycle, the alignment of the X-rays, lasers, and temperature measurement system was verified according to the procedure described in Anzellini et al.[27] The heating cycles were performed in "trigger mode": both lasers were set to a target power, and after 0.3 s, a diffraction pattern and a T measurement were simultaneously recorded. Then, 0.3 s after the X-ray diffraction (XRD) collection, both laser powers were reset to zero, and a new XRD pattern from the quenched sample was collected. This procedure minimized the laser-sample interaction time (reducing the potential for chemical reactions) and allowed for optical adjustments as needed. During each heating cycle, the laser powers were increased until a diffuse signal (indicative of melting) was observed in the diffraction pattern, or until no further temperature increase was possible, likely due to changes in the sample's insulating properties, such as the formation of a laser-drilled hole. Several heating cycles were performed on the same samples at different $P-T$ conditions. To prevent chemical contamination, each cycle was conducted on a fresh region of the sample, and the quality of the chosen region was first checked using XRD before heating.

Data analysis

During the data analysis, careful attention was paid to various aspects of the experiment. Temperature measurements were cross-checked following the method in Benedetti and Loubeyre[51]. A detailed analysis of the diffraction patterns was performed to identify melting and to obtain structural and textural information about the sample and the insulating material.

The presence of a diffuse X-ray scattering contribution served as an in situ indicator of high-pressure melting during the experiment. Diffuse X-ray scattering from the liquid appeared as a continuous, isotropic signal across the image plate. In contrast, thermal diffusion from the hot, solid portion of the sample manifested as broad, yet distinct, diffraction spots. To precisely determine the onset of melting, we followed the procedure outlined by Morard et al.[52]. We confirmed the presence of melting, by integrating selected portions of the image plate with a minimum contribution from the thermal diffusion from the single crystal spots.

For both the RH and LH-DAC experiments, masks were applied to each image, and the images were azimuthally integrated using the DIOPTAS software suite[45]. The Ir data were treated as powder diffraction data for the RH experiment and a Pawley refinement was performed using the TOPAS software[53] with previously reported parameters as initial values. A similar analysis was performed for the XRD data obtained from the laser-heating experiment at T below recrystallization. Above recrystallization, the XRD patterns were treated as single-crystal data; in this case, a single Ir peak was tracked during heating and individually integrated to determine its lattice parameter. This approach was feasible due to Ir's cubic structure, where a single peak is sufficient for lattice parameter extraction. Data scatter is attributed to temperature gradients within the scanned region. Finally, the structural measurements were compared to the T ones so to obtain a detailed in situ and "time-resolved" analysis of the sample evolution as a function of P and T. The obtained volumetric compression as a function of P and T were analysed with the EOSfit software suite[38] so to extract the corresponding equation of states.

Data availability

The authors declare that the data supporting the findings of this study are available within the paper and its Supplementary Material.

References

1. Wang, W., Dong, C. & Shek, C. Bulk metallic glasses. *Mater. Sci. Eng. R Rep.* **44**, 45–89 (2004).
2. Motta, A. T. et al. Zirconium alloys for supercritical water reactor applications: challenges and possibilities. *J. Nucl. Mater.* **371**, 61–75 (2007).
3. Anzellini, S., Dewaele, A., Mezouar, M., Loubeyre, P. & Morard, G. Melting of iron at Earth's inner core boundary based on fast X-ray diffraction. *Science* **340**, 464–6 (2013).
4. Liu, J., Li, J., Hrubiak, R. & Smith, J. S. Origins of ultralow velocity zones through slab-derived metallic melt. *Proc. Natl. Acad. Sci.* **113**, 5547–5551 (2016).
5. Poirier, J.-P. *Introduction to the Physics of the Earth's Interior* (Cambridge University Press, 2003).
6. Morard, G. et al. Structure of eutectic Fe-FeS melts to pressures up to 17 GPa: implications for planetary cores. *Earth Planet. Sci. Lett.* **263**, 128–139 (2007).
7. Miozzi, F. et al. Eutectic melting of Fe-3 at% Si-4 at% C up to 200 GPa and implications for the Earth's core. *Earth Planet. Sci. Lett.* **544**, 116382 (2020).
8. Hirose, K., Labrosse, S. & Hernlund, J. Composition and state of the core. *Annu. Rev. Earth Planet. Sci.* **41**, 657–691 (2013).
9. Alfè, D., Kresse, G. & Gillan, M. Structure and dynamics of liquid iron under Earth's core conditions. *Phys. Rev. B* **61**, 132–142 (2000).
10. Cerenius, Y. & Dubrovinsky, L. Compressibility measurements on iridium. *J. Alloy. Compd.* **306**, 26 (2000).
11. Burakovsky, L., Preston, D. L. & Errandonea, D. Ab initio study of randomly disordered hexagonal close-packed (rhcp) phase in platinum. *J. Appl. Phys.* **137**, 015109 (2025).
12. Monteseguro, V. et al. Phase stability and electronic structure of iridium metal at the megabar range. *Sci. Rep.* **9**, 8940 (2019).
13. Burakovsky, L. et al. Ab initio phase diagram of iridium. *Phys. Rev. B* **94**, 094112 (2016).
14. Yusenko, K. et al. Equations of state of rhodium, iridium and their alloys up to 70 GPa. *J. Alloy. Compd.* **788**, 212 (2019).
15. Tal, A. et al. Pressure-induced crossing of the core level in 5d metals. *Phys. Rev. B* **93**, 205150 (2016).
16. Storm, C. et al. Experimental and computational study of the core-level crossing transition in iridium at high pressure. *Phys. Rev. B* **109**, 024101 (2024).
17. Smirnov, N. Ab initio calculations of structural stability, thermodynamic and elastic properties of Ni, Pd, Rh, and Ir at high pressures. *J. Appl. Phys.* **14**, 025901 (2023).
18. Nemoshkalenko, V., Milman, V., Zhalko-Titarenko, A., Antonov, V. & Shitikov, Y. Dynamics of the iridium lattice: experiment and calculations. *Pisma Zh. Eksp. Teor. Fiz.* **47**, 295 (1988).
19. Cynn, H., Klepeis, J. E., Yoo, C.-S. & Young, D. A. Osmium has the lowest experimentally determined compressibility. *Phys. Rev. Lett.* **88**, 676 (2002).
20. Anzellini, S., Burakovsky, L., Turnbull, R., Bandiello, E. & Errandonea, D. P-V-T equation of state of iridium up to 80 GPa and 3100 K. *Crystals* **11**, 452 (2021).
21. Akella, J. High-pressure studies on iridium to 30.0 GPa. *J. Phys. Chem. Solids* **43**, 941 (1982).
22. Han, J., Shi, L.-Q., Wang, N., Zhang, H.-F. & Peng, S.-M. Equation of state of Iridium: from insight of ensemble theory. *J. Phys.: Condens. Matter* **34**, 465702 (2022).
23. Brown, J., Davis, J. & Seagle, C. Multi-megabar dynamic strength measurements of Ta, Au, Pt, and Ir. *J. Dyn. Behav. Mater.* **7**, 196 (2021).
24. Thakur, B., Gong, X. & Corso, A. D. Ab initio thermodynamic properties of iridium: a high-pressure and high-temperature study. *Comput. Mater. Sci.* **234**, 112797 (2024).
25. Luo, K., Lu, R. & Cohen, R. First-principles thermal equation of state of fcc iridium. *Phys. Rev. B* **107**, 014106 (2023).
26. Lord, O. et al. The melting curve of Ni to 1 Mbar. *Earth Planet. Sci. Lett.* **408**, 226–236 (2014).
27. Anzellini, S. et al. In situ characterization of the high pressure- high temperature melting curve of platinum. *Sci. Rep.* **9**, 13034 (2019).
28. Anzellini, S., Alfé, D., Pozzo, M. & Errandonea, D. Melting line of calcium characterized by in situ LH-DAC XRD and first-principle calculations. *Sci. Rep.* **11**, 15025 (2021).
29. Anzellini, S. et al. Melting line and thermal equation of state of fcc-cobalt: a combined experimental and computational approach. *Results Phys.* **56**, 107218 (2024).
30. Anzellini, S. et al. Characterization of the high pressure and high-temperature phase diagram and equation of state of chromium. *Sci. Rep.* **12**, 6727 (2022).
31. Kimura, T., Ohfuji, H., Nishi, M. & Irifune, T. Melting temperatures of MgO under high pressure by micro-texture analysis. *Nat. Commun.* **8**, 15735 (2017).
32. Boehler, R., Ross, M. & Boerker, D. High-pressure melting curves of alkali halides. *Phys. Rev. B* **53**, 556 (1996).
33. Pistorius, C. Melting curves of the potassium halides at high pressures. *J. Phys. Chem. Solids* **26**, 1543 (1965).
34. Snellings, R., Salze, A. & Scrivener, K. Use of X-ray diffraction to quantify amorphous supplementary cementitious materials in anhydrous and hydrated blended cements. *Cem. Concr. Res.* **64**, 89 (2014).
35. Zhou, D., Dong, J., Si, Y., Zhu, F. & Li, J. Melting curve of potassium chloride from in situ ionic conduction measurements. *Minerals* **10**, 250 (2020).
36. Slifka, A. J., Filla, B. J. & Phelps, J. M. Thermal conductivity of magnesium oxide from absolute, steady-state measurements. *J. Res. Natl. Inst. Stand. Technol.* **103**, 357 (1998).
37. Slack, G. A. Thermal conductivity of potassium chloride crystals containing calcium. *Phys. Rev.* **105**, 832 (1957).
38. Angel, R. J., Gonzalez-platas, J. & Alvaro, M. EosFit7c and a Fortran module (library) for equation of state calculations. *Z. Kristallogr.* **229**, 405–419 (2014).
39. Zha, C.-S. et al. P-V-T equation of state of platinum to 80 GPa and 1900 K from internal resistive heating/X-ray diffraction measurements. *J. Appl. Phys.* **103**, 054908 (2008).
40. Anzellini, S. et al. Phase diagram of ruthenium characterized in situ by synchrotron X-ray diffraction and ab initio simulations. *Results Phys.* **65**, 107961 (2024).
41. Letoullec, R., Pinceaux, J. P. & Loubeyre, P. The membrane diamond anvil cell: a new device for generating continuous pressure and temperature variations. *High. Press. Res.* **1**, 77–90 (1988).
42. Boehler, R. & Hantsetters, K. D. New anvil designs in diamond-cells. *High. Press. Res.* **24**, 391 (2004).
43. Garbarino, G. et al. Extreme conditions X-ray diffraction and imaging beamline ID15B on the ESRF extremely brilliant source. *High. Press. Res.* **44**, 199–216 (2024).
44. Anzellini, S. et al. Laser-heating system for high-pressure X-ray diffraction at the extreme condition beamline I15 at Diamond Light Source. *J. Synchrotron Radiat.* **25**, 1860–1868 (2018).
45. Prescher, C. & Prakapenka, V. DIOPTAS: a program for reduction of two-dimensional X-ray diffraction data and data exploration. *High. Press. Res.* **35**, 223 (2015).
46. Rosa, A. et al. Amorphous boron composite gaskets for in situ high-pressure and high-temperature studies. *High. Press. Res.* **36**, 564 (2016).
47. Dewaele, A. et al. High-pressure-high-temperature equation of state of KCl and KBr. *Phys. Rev. B Condens. Matter Mater. Phys.* **85**, 1–7 (2012).
48. Speziale, S., Zha, C., Duffy, T., R.J, H. & Mao, H. Quasi-hydrostatic compression of magnesium oxide to 52 GPa: Implications for the pressure-volume-temperature equation of state. *J. Geophys. Res.* **106**, 515 (2001).

49. Anzellini, S. & Boccato, S. A practical review of the laser-heated diamond anvil cell for university laboratories and synchrotron applications. *Crystals* **10**, 459 (2020).

50. Louvel, M. et al. The HXD95: a modified Bassett-type hydrothermal diamond-anvil cell for in situ XRD experiments up to 5 GPa and 1300 K. *J. Synchrotron Radiat.* **27**, 529 (2020).

51. Benedetti, L. & Loubeyre, P. Temperature gradients, wavelength-dependent emissivity, and accuracy of high and very-high temperatures measured in the laser-heated diamond cell. *High. Press. Res.* **24**, 423–445 (2004).

52. Morard, G. et al. Melting of Fe Ni Si and Fe Ni S alloys at megabar pressures: implications for the core mantle boundary temperature. *Phys. Chem. Miner.* **38**, 767–776 (2011).

53. Coelho, A. TOPAS and TOPAS-Academic: an optimization program integrating computer algebra and crystallographic object written in C ++. *J. Appl. Crystallogr.* **51**, 210 (2018).

54. McHardy, J. et al. Thermal equation of state of rhodium to 191 GPa and 2700 K using double-sided flash laser heating in a diamond anvil cell. *Phys. Rev. B* **109**, 094113 (2024).

55. Young, D. *Phase Diagram of the Elements* (University of California Press, 1991).

Acknowledgements

Author contributions

S.A. and D.E. conceived the experiment. S.A., P.B., J.L.R.R., A.G.B., J.S.M, G.G., A.D.R., S.G.P., and E.K. performed the experiment. S.A. analysed the data. D.E. and S.A. provided funding. The paper was written through the contribution of all authors.

Competing interests

The authors declare no competing interests.

Additional information

Supplementary information The online version contains supplementary material available at https://doi.org/10.1038/s43246-025-00963-4.

Correspondence and requests for materials should be addressed to Simone Anzellini.

Peer review information *Communications Materials* thanks the anonymous reviewers for their contribution to the peer review of this work.

Reprints and permissions information is available at http://www.nature.com/reprints

Publisher's note Springer Nature remains neutral with regard to jurisdictional claims in published maps and institutional affiliations.